

<https://doi.org/10.1038/s43246-025-00819-x>

# Metal flow mechanisms during alternating current arc welding and additive manufacturing of aluminium alloy



Bin Xu<sup>1</sup>, Chengyu Zhang<sup>1</sup>, Guokai Zhang<sup>1</sup>, Fan Jiang<sup>1</sup> , Shinichi Tashiro<sup>2</sup>, Manabu Tanaka<sup>2</sup> & Shujun Chen<sup>1,3</sup>

Alternating current (AC) arc melting technology has been developed for the manufacturing of lightweight materials and provides a potential heat source in welding and additive manufacturing. However, metal flow and the corresponding effects of AC arc melting remain unclear. Here, 3D internal and surface flows in an aluminium alloy during AC tungsten arc melting are studied via in situ/operando 4D X-ray radiography and laser high-speed imaging. The molten flow velocity under positive polarity is much greater than that under negative polarity. We find that liquid metal flow is mainly influenced by the cathode spot motion at the molten pool surface in the electrode positive stage. This information can be used to guide process optimization in the manufacturing of light metals via AC arc melting.

Aluminium, magnesium, and their alloys are widely used in aerospace, automotive, rail transit, electrical and electronic applications for energy savings, as well as for parts that operate at high speeds and thus must be lightweight to minimize inertial forces<sup>1,2</sup>. Processing methods such as welding and additive manufacturing are indispensable in the manufacture of light alloy structures<sup>3</sup>. Among them, the gas tungsten alternate current (AC) arc, as a typical heat source for processing of aluminium alloys and magnesium alloys, has many advantages such as lack of spatter, limited smoke, relatively high stability and high quality, as well as ability to clean oxide film by cathode spots<sup>4–6</sup>. The molten pool dynamics resulting from arc melting have been shown to be strongly related to be quality and mechanical properties of the manufactured product. However, even after decades of development, the complex physics of molten pool flows from AC arc melting still cannot be understood clearly because of many unresolved issues such as cathode spots, arc forces, and heat transport.

In recent years, with the development of hardware such as high-speed video cameras<sup>7–9</sup>, X-ray devices<sup>10–12</sup> and high-energy synchrotron radiation<sup>13–19</sup>, as well as software for imaging and data processing<sup>20,21</sup>, the visualization of molten pool dynamics has improved. In addition to experimental observations, significant efforts towards computational modelling have been made to better understand molten pool flow<sup>22–26</sup>. It is generally believed that the convective fluid flow in a molten pool is influenced by the balance among buoyancy, the viscous drag force, the thermocapillary force and the Lorentz magnetic pressure. The system may be dominated by the drag force from the cathode jet or the Marangoni effect, which varies depending on different conditions such as the composition of the shielding gas, molten pool size and arc length. Rough

experiments can be used to guide these models<sup>27,28</sup>. AC arc melting can be classified into two types: one where both electrodes melt<sup>29–31</sup> and the other where only one electrode melts (the non-melting electrode material is mainly tungsten)<sup>32,33</sup>. Even though the AC gas tungsten arc is relatively stable because there is no droplet transfer, the variations of tungsten melting and cathode spot jumping under polarity switching govern the thermal and force outputs<sup>4,34,35</sup>. Spots on a cold cathode, as a typical feature of electrode-positive (EP) polarity, create receptive craters with current densities  $>10^{11} \text{ A m}^{-2}$  and power flux densities exceeding  $10^{12} \text{ W m}^{-2}$ . The high-speed motion of a cold cathode surface is one of the most intriguing characteristics of such structures<sup>36–41</sup>. Shielding gas, metal vapour, and the molten pool temperature are presumed to affect spot behaviour, but conclusions remain unclear<sup>42,43</sup>. The energy and momentum balance on the interface during AC arc melting is poorly understood; thus, heat transfer and fluid flow are controversial<sup>44–47</sup>.

This work focuses on liquid metal flow under different polarities during the process of melting with an AC tungsten arc. A laser and high-speed imaging system and dual X-ray radiography (DXR), were used to observe the surface and internal flow of the molten pool. Tracer particles in time-dependent images were used to quantify the liquid metal flow in situ and operando. Regardless of the molten pool state, a pronounced difference in flow velocity between the EP and electrode negative (EN) stages is observed during AC arc melting of aluminium alloy. This difference is closely associated with the aggregation and motion of cathode spots during the EP stage. The increasingly complex melting of lightweight metals can be optimized by better understanding molten pool dynamics during AC arc use to enhance manufacturing quality.

<sup>1</sup>College of Mechanical & Energy Engineering, Beijing University of Technology, 100124 Beijing, China. <sup>2</sup>Joining and Welding Research Institute, Osaka University, Osaka, 5670047, Japan. <sup>3</sup>Institute of Matter Science (Huairou), Beijing University of Technology, 100124 Beijing, China. e-mail: [jiangfan@bjut.edu.cn](mailto:jiangfan@bjut.edu.cn); [sjchen@bjut.edu.cn](mailto:sjchen@bjut.edu.cn)

## Results

### Surface flow of a molten pool with AC arc melting

There are three basic types of tungsten gas arc melting, and a schematic is shown in Fig. 1a. A tungsten inert gas (TIG) arc is a type of free-burning arc with a low energy density. The depth of the melt is shallow and there is little deformation of the gas-liquid surface. The plasma arc is constrained by a water cooling nozzle, which has a relatively high heat flux, plasma flow velocity and arc forces, resulting in a large melting depth and deformation of the molten pool surface<sup>48,49</sup>. According to whether there is full perforation, the plasma arc melting can be divided into two types: one with a molten pool with a blind keyhole formed by soft plasma arc (SPA) and one with a keyhole molten pool formed by a keyhole plasma arc (KPA). When melting aluminium alloys, it is necessary to utilize the characteristics of AC arcs to clean the oxide film on the workpiece surface. Therefore, the plasma arc investigated here is an AC plasma arc with a rectangular AC waveform, commonly referred to as a variable polarity plasma arc (VPPA).

The positions of the high-speed camera and the welding torch are fixed. Prior to welding, a steel ruler is placed directly beneath the welding torch and a single image is captured to calibrate the two-dimensional coordinate system, facilitating the calculation of the molten pool dimensions during the welding process. The origin of the coordinate system is set at the centre of the weld seam. The aluminium alloy plate is fixed on a mobile trolley. In this work, zirconia particles with a diameter of 0.03 mm are used as tracer

particles and are pre-embedded during the melting process. With a melting point of 2973 K, zirconia does not react chemically with the aluminium alloy. In the images, the solid particles adhere to the surface of the molten pool and move concurrently with the molten metal.

A high-speed camera and laser with a 520 nm wavelength were used to visualize the molten pool of the TIG arc perpendicular to the melting direction (Fig. 1b). When  $y = 0$ , the flow velocity along the  $x$  direction was calculated, which clearly shows that the flow velocity in the EP stage is significantly higher than that in EN stage (Supplementary Movie 1). The velocity in the EP stage is approximately  $10\text{--}20\text{ mm s}^{-1}$ , with an average velocity lower than  $10\text{ mm s}^{-1}$ . This value is much lower than the flow velocity of the direct current (DC) TIG molten pool. During plasma arc melting, the flow of the rear side of the molten pool, which is important for bead formation, is observed in the melting direction. The curve in Fig. 1c shows the flow velocity along the  $y$  direction when  $x = 0$ . In the molten pool with a blind keyhole, the flow velocity in the EP stage is also greater than that in the EN stage (Supplementary Movie 2). The maximum velocity in the EP stage is approximately  $40\text{ mm s}^{-1}$ , which is slightly higher than that in the TIG arc melting process. The average velocity is approximately  $10\text{ mm s}^{-1}$ , which is close to that of TIG. As shown in Fig. 1d, the fusion zone obtained in the KPA melting process is significantly different from that in the other processes. The workpiece is completely penetrated and the required energy is correspondingly greater. Additionally, the flow velocity in the EP stage is

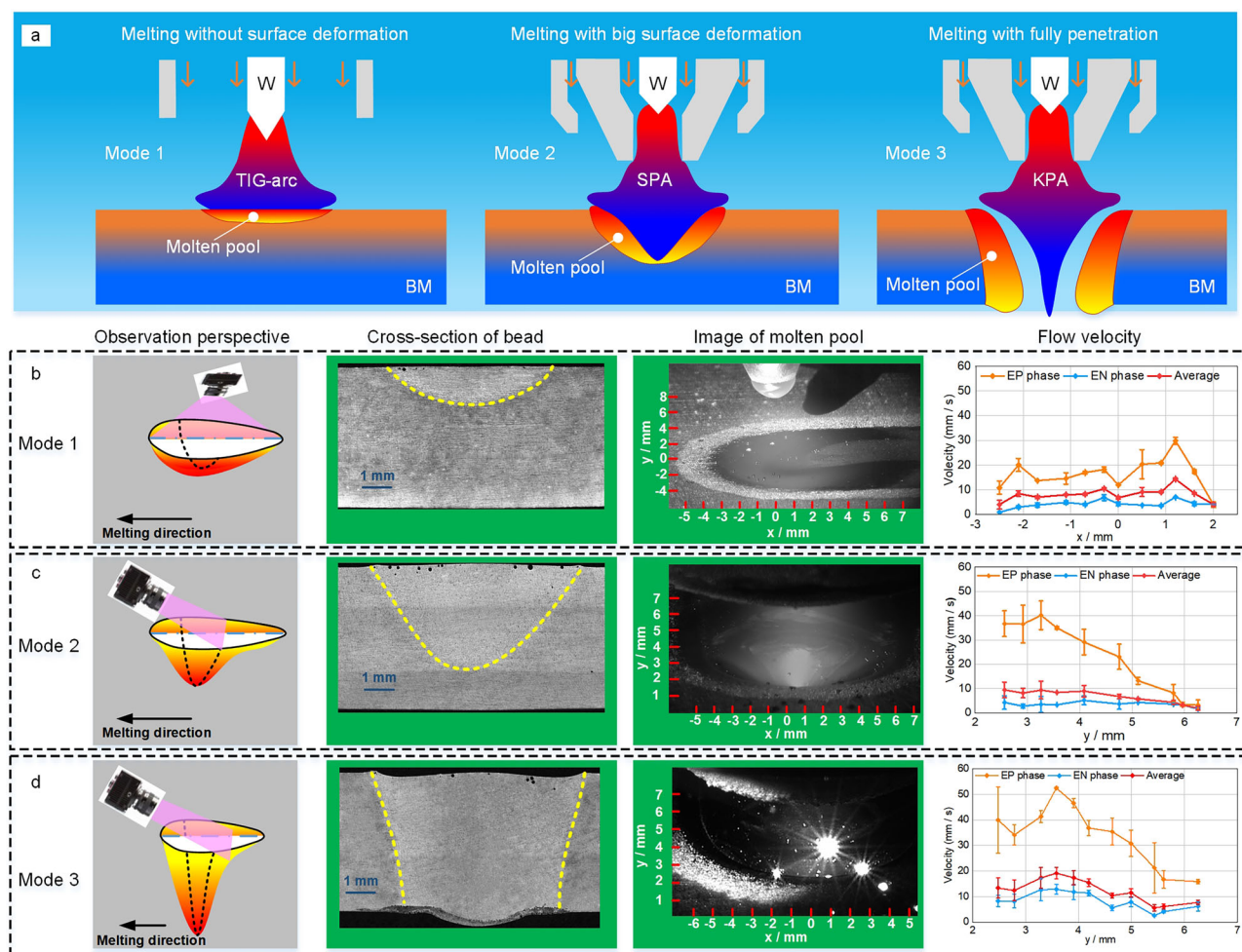


**Fig. 1 | Three different types of tungsten gas arc melting and observation of molten pool flow.** **a** Schematic illustrating the structure formed when tungsten is used as the electrode material to create an arc for melting aluminium alloy. Under the thermal and force effect of the arc, the metal undergoes melting and deformation, which can be categorized into three main forms. **b** The observation angle of the high-speed camera and the flow velocity under EP and EN polarities during the TIG arc

melting of aluminium alloy. The camera observation path is perpendicular to the melting direction. **c** Plasma arc melting process with a blind keyhole. The camera observes facing the melting direction. **d** Plasma arc melting process with a keyhole. Error bars represent one standard deviation (SD) from the mean. TIG-arc tungsten inert gas arc, SPA soft plasma arc, KPA keyhole plasma arc.

still higher than that in the EN stage (Supplementary Movie 3). This finding indicates that regardless of how the arc and molten pool state change, if the arc is an AC tungsten electrode arc, the liquid metal flow velocity in the EP section of the current cycle during the melting process is much greater than that in the EN stage, which is a unique phenomenon. Compared with TIG arcs, plasma arcs are more constricted and exhibit a higher arc temperature, resulting in more complete ionization of the gas medium and higher current densities. Microscopically, particle collisions within the plasma arc involve processes of energy absorption and release. The arc temperature is primarily related to Joule heating and heat from microscopic particle collisions. Gas constriction by the plasma arc increases the particle velocity and collision frequency, enhancing ionization and energy release in the arc region<sup>50,51</sup>. Consequently, plasma arcs exhibit higher temperatures and flow rates than do TIG arcs. However, when applied to a melted aluminium alloy, the average flow velocity of the molten pool metal is essentially similar, as will be discussed.

### Measurement of the flow on the whole keyhole molten pool surface

It is difficult to obtain the whole surface flow of a keyhole molten pool with a laser and a High-speed video camera (HSVC). The DXR device shown in Fig. 2a can pass through the area of the keyhole molten pool and be imaged by the camera. This device enables the acquisition of the three-dimensional coordinates of tracer particles. Aucott et al.<sup>28</sup> emphasized that two-dimensional imaging lacks accuracy in quantifying the flow velocity of the molten pools. Currently, all synchrotron imaging techniques provide only two-dimensional projections. Therefore, the device used in this study offers a significant advantage in accurately quantifying the flow velocity within the molten pools. The movement of small bubbles in a molten pool can reflect metal flow, but it is difficult to capture the flow at the gas-liquid interface because the bubbles tend to rupture and release gas when approaching the interface<sup>14,15</sup>. The aluminium alloy plate is a cuboid with a size of length  $\times$  width  $\times$  thickness of 150 mm  $\times$  100 mm  $\times$  mm, as shown in Fig. 2b. The AC plasma arc melts and penetrates the solid metal to form the keyhole molten pool, which then moves in the length direction. The keyhole molten pool produced by the VPPA can be divided into 6 typical positions. A schematic of the keyhole section with different locations marking is shown in Fig. 2c. Achieving upwards flow at the back, top and surface positions is the key to successful welding<sup>52</sup>.

The intersection of the two X-rays is fixed. The spatial position coordinate system is subsequently calibrated using a plastic plate with holes engraved at a fixed distance. The flow velocity can be calculated using the spatial coordinates and internal time between the images (as shown in Figs. 2d–g). The aluminium alloy plate is fixed on the mobile trolley. The heights of the torch and workpiece are adjusted on the basis of the position of the keyhole on the monitor. The detection process steps are as follows. The trolley is moved to the starting position, the arc is started, the plasma arc melts the metal, and the trolley is started when the workpiece is almost penetrated. When the tracer particles enter the field of view, the high-speed camera is triggered, and the image is collected and saved. X-ray radiographs of the molten region, illustrated in Fig. 2e, were captured by HSVC at a 2 kHz frame rates, covering the whole region of keyhole and molten pool. Tungsten (W) balls with a diameter of 0.3 mm, pre-embedded in the melting route in advance, were employed as tracer particles. The solid particles are darker than the surrounding liquid metal in the image because W has much greater X-ray attenuation than the liquid metal. We used tungsten particles pre-embedded in the welding path as tracer particles. By embedding multiple tracer particles at different positions and depths, we obtained various flow trajectories. The W particles have an insignificant effect on the flow patterns and velocities in liquid metal as the sinking speed can be considered negligible<sup>28</sup>. If a tracer particle enters the deeper regions of a molten pool, it provides information on internal flow, whereas if a tracer particle adheres to the surface of the molten pool, it reflects the surface flow. In summary, zirconia can be used to measure only the surface flow of a molten pool, whereas tungsten particles can capture both the internal and

surface flows. When different methods are used to detect molten pool flow and compare and verify the results, the accuracy and reliability of the data can be enhanced.

Figure 2h shows the enlargement of the keyhole region at the beginning of the EN stage, showing the relative position of the particles. For the area labelled with a red dotted line, as shown in Fig. 2i, the movement of particles with different polarities can be clearly observed over one current cycle. In the EN stage (from 0.0 to 12.5 ms), the positions of the particles remain almost unchanged. From the beginning of the EP stage (14.5 ms) to the end (21.0 ms), the movement of the particles by  $\Delta t$  is very distinct. This phenomenon is consistent with the detection of surface flow. This phenomenon is further explained in the Supplementary Movie 4.

### Internal convection of the keyhole molten pool by an AC plasma arc

On the basis of the images captured by high-speed cameras, the coordinates of the tracer particles during their movement can be obtained. The flow velocities of liquid metals at each polarity can be calculated on the basis of the particle position and duration for the EN and EP cases (Fig. 3). There are two typical flow trajectories of the keyhole molten pool: surface upwards flow (red colour) and internal flow (blue colour) after detouring the keyhole. Figure 3a–c shows the flow trajectories in the melting process of plates with sizes of 5, 8 and 10 mm, respectively. The difference in trajectories is likely due to the differences in the molten pool size and keyhole morphology with different plate melting thicknesses. A particle moving along the internal trajectory travels along the keyhole wall first and then enters the deep region of the trailing molten pool behind the keyhole. When it is near the keyhole wall, its velocity in the EP stage is much greater than that in the EN stage, as shown in Fig. 3d, which is consistent with the results of the molten pool surface flow measurement shown in Fig. 1. The velocity in the EN stage begins to increase when the particle enters a deep position in the melt pool, whereas the velocity in the EP stage decreases until the velocities of the two stages approach each other. For the velocity along a surface trajectory with a plate thickness of 5 mm, the velocity in the EP stage is approximately 30 mm s<sup>-1</sup>, which is higher than that in the EN stage. The same phenomenon occurs in the 8 and 10 mm cases, where the flow velocity in the EP stage is higher than that in the EN stage on the keyhole wall surface, whereas the flow velocities under positive and negative polarities are similar at the deep position in the melt pool.

### Discussion

In summary, there is a significant difference in the flow velocity of the molten pool between the EN and EP stages when approaching the surface of the molten pool. The flow velocity in the EN stage is very low. In recent years, some studies have suggested that the flow of the molten pool created by a tungsten arc is mainly dominated by the drag force from the cathode jet<sup>11,53,54</sup>. Similarly, the deformation of the gas-liquid interface during digging the process of keyhole welding by a DC plasma arc is dominated by this mechanism<sup>55</sup>. The digging process is the initial stage of plasma arc keyhole welding, during which the molten pool surface progressively deforms into a concave shape, eventually leading to full penetration of the workpiece<sup>56</sup>. In the EN stage of AC arc melting, the arc is concentrated because all the electrons are emitted from the tungsten tip, which causes the current density, arc temperature, pressure and plasma flow velocity to be greater than those in the EP stage; thus, the abovementioned arc drag force from the cathode jet is greater. If the molten pool flow is affected mainly by this force, as noted in previous studies, the flow velocity during the EN stage should be higher than that during the EP stage. However, this is obviously contradictory to the actual experimental observations in our work. Therefore, we can infer that there must be a new influencing mechanism in the metal flow during the process of AC arc melting.

$$\tau = \mu \frac{u_a - u_l}{d} \quad (1)$$



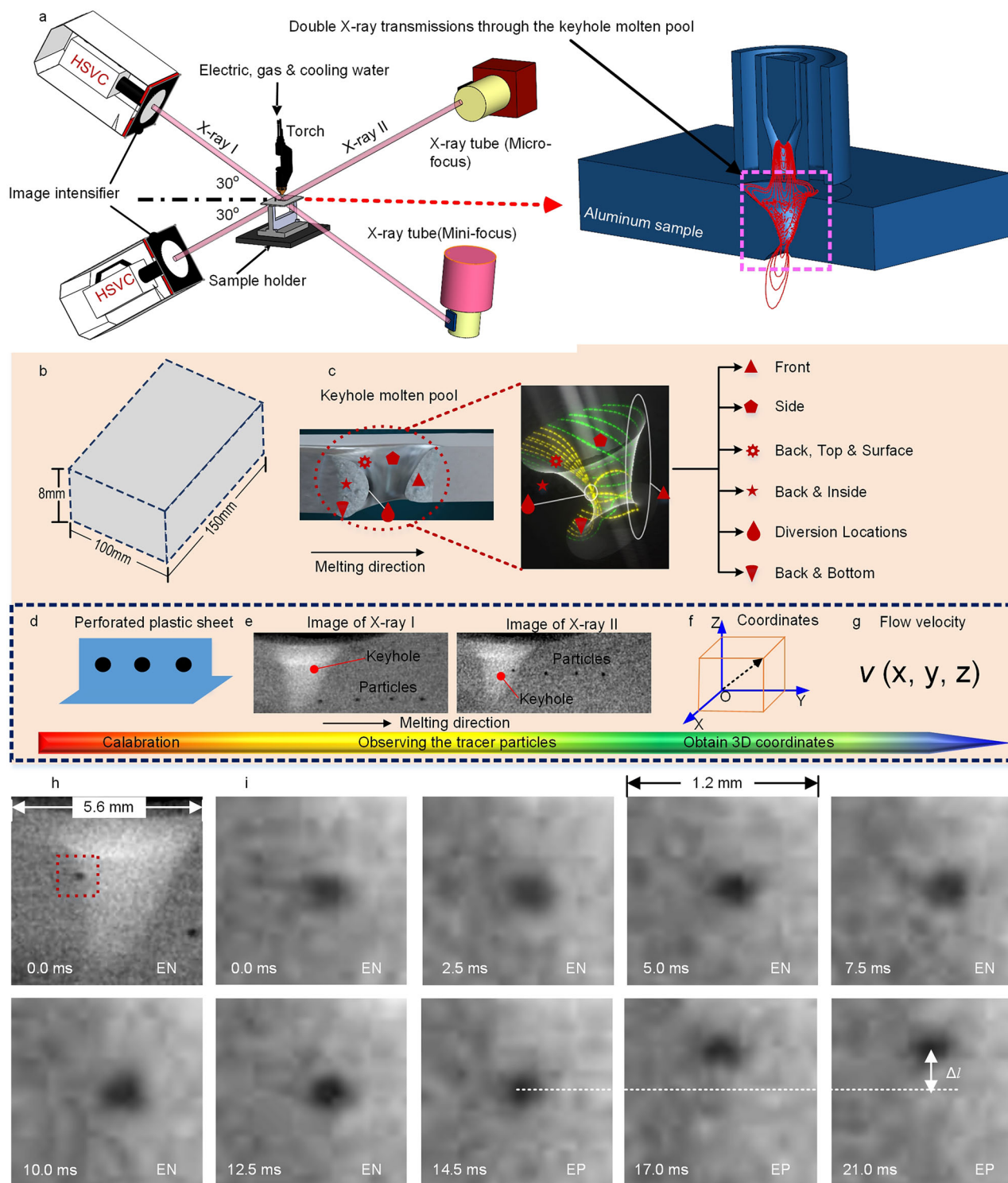


**Fig. 2 | Four-dimensional in situ / operando radiography of a keyhole molten pool flow with dual X-ray sources system.** **a** Schematic of the relative position between the dual X-ray imaging system and the heat source melting device. The plasma arc forms a keyhole molten pool, where the two X-ray beams transmitted through. **b** Schematic of aluminium alloy plate. The shown thickness is 8 mm, with 5 mm and 10 mm also included (see “Methods” section for details). The dimensions are not to scale. **c** Different locations of keyhole molten pool. The keyhole molten

pool is a “cylindrical” liquid metal with a hole in the middle, divided into six typical regions. **d** Plastic plate for calibration. The plate is placed at different positions and perform X-ray imaging before experiment. Spatial coordinate is calibrated based on the position of the hole in the images. **e** Images obtained with the two X-ray devices and HSVCs. **f** Coordinates of the particle. **g** Velocity calculation. **h** Magnification of the keyhole region with a particle. The tungsten ball is inside the dashed box. **i** Particle motion in one period. HSVC: High-speed video camera.

In addition, the flow velocity ( $u_a$ ) of the arc plasma close to the surface of the melt pool is approximately  $200 \text{ m s}^{-1}$  as shown in Fig. 4, which is much higher than that of molten metal ( $u_l$ ). The dynamic viscosity ( $\mu$ ) of the plasma is approximately  $10^{-5} \text{ kg m}^{-1} \text{ s}^{-1}$ . The thickness ( $d$ ) of the gas-liquid

boundary layer is  $1 \text{ }\mu\text{m}$  at minimum. Equation (1) shows that the arc shear force ( $\tau$ ) generated by the arc plasma jet is approximately  $10^3 \text{ N m}^{-2}$  which is much smaller than the atmospheric pressure of  $10^5 \text{ N m}^{-2}$ . Therefore, its effect on the metal liquid surface should be very weak<sup>57</sup>. Assuming that the

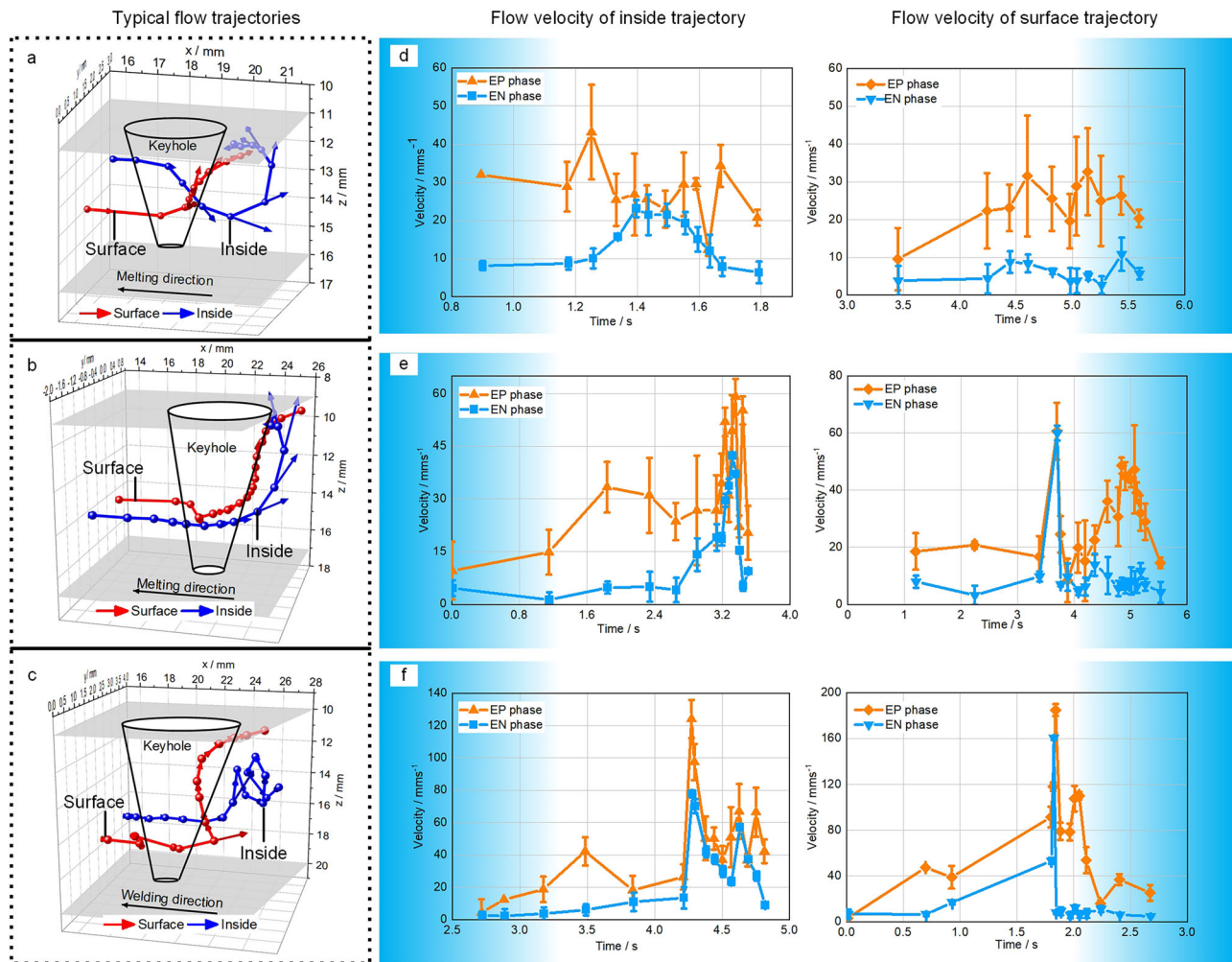
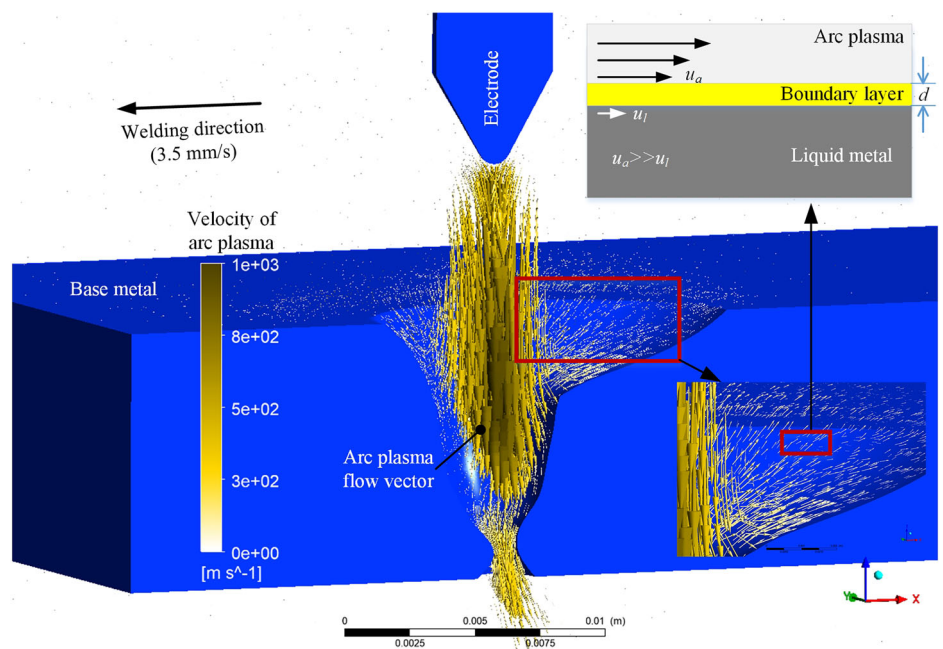


**Fig. 3 | Analysis of surface and internal flow velocity of the keyhole molten pool.** The flow velocity of EN and EP on the trajectory of a single tracer particle calculated from X-ray imaging. **a–c** Trajectories on the surface (red colour) and inside (blue

colour). **d–f** Flow velocity of EP and EN stage on the two trajectories. The thicknesses of base metal are 5 mm (**a, d**), 8 mm (**b, e**), 10 mm (**c, f**). Error bars represent one standard deviation (SD) from the mean.

**Fig. 4 | The flow vector of the arc plasma on the surface of the keyhole molten pool obtained via numerical simulation.**  $u_a$  is the flow velocity of the arc plasma.  $u_l$  is the flow velocity of liquid metal in molten metal.  $\mu$  is the dynamic viscosity of the arc plasma.  $d$  is the thickness of the gas-liquid boundary layer.



liquid surface is stationary, the internal pressure of the liquid equals atmospheric pressure. If the shear force is able to drive metal flow and generate velocity, according to Bernoulli's equation, the pressure term will decrease and the kinetic energy term will increase. This disrupts the equilibrium of the liquid surface, leading to undulations or concave deformations, meaning that the shear force works against the pressure term. Therefore, if the shear force is capable of driving metal flow, its magnitude would need to be on the order of atmospheric pressure. Since the arc plasma generates only a small shear force due to its very low viscosity, it is difficult for it to drive metal flow.

The numerical simulations mentioned in the article pertain to the velocity of the arc plasma, whereas the experimental measurements focus on the velocity of the molten metal in the molten pool. Naturally, there is a significant difference between the two. The reason for the high velocity of the arc plasma is that, despite its high flow velocity, the arc plasma, owing to its low viscosity and low density, cannot drive the flow of the molten metal. This is also the reason why the Kelvin-Helmholtz instability<sup>58</sup> is not induced, despite the significant difference between the flow velocity of the arc plasma and that of the metal in the molten pool.

To further experimentally explore whether the arc shear force has a major impact on the above system, we designed an experiment to vary the arc confinement state and thus vary the plasma flow velocity. Figure 5a shows the three-dimensional fluid flow of the keyhole molten pool with different tungsten setbacks. The plasma arc is increasingly constricted with greater tungsten setback, which makes the arc plasma flow faster; thus, the arc force and pressure are high. The red vector arrows in the figure represent the liquid-metal flow velocity. Figure 5a shows the results for a 2 mm tungsten setback. On the front side of the keyhole, the liquid metal flows from the bottom side to the top side. On the sidewall of the keyhole, the liquid metal flows upwards while flowing to the rear of the weld direction. In the keyhole bottom region, some liquid metal flows downwards. The flow patterns are basically the same in the 2 mm case as those for the 4 and 6 mm tungsten setbacks. The metal that detoured the keyhole and flows into the middle of the weld bead is mainly from the bottom region of the keyhole. The metal detours the keyhole at the bottom region and then enters the trailing molten pool. The upwards flow velocity of the liquid metal in the keyhole molten pool on the trailing side shows little difference with changes in the tungsten setback (Fig. 5b), indicating that although the arc state and force change, they do not significantly affect the liquid metal flow. Thus, there is a non-variable factor affecting the melt pool flow.

In addition, it is generally believed that the surface tension gradient in the tangential direction caused by the temperature difference on the surface of the melt pool, namely the so-called Marangoni force, is another important factor affecting the flow of the melt pool. Especially for the welding or additive manufacturing processes of ferrous metals, flow detection has clearly demonstrated that the Marangoni force dominates the flow<sup>14,28</sup>, which may be due to the large surface tension gradient and temperature gradient. However, for aluminium alloys, obtaining reliable evidence to study the effect of the Marangoni force is difficult because an oxide film generally forms on the surface of aluminium alloys, making accurate measurement of surface tension challenging.

In many numerical simulation studies, different values have been adopted for the surface tension gradient of aluminium alloys. In some cases<sup>59,60</sup>, it is set to  $-3.5 \times 10^{-4} \text{ N m}^{-1} \text{ K}^{-1}$ , whereas in other cases<sup>61</sup>, a value of  $-0.5 \times 10^{-4} \text{ N m}^{-1} \text{ K}^{-1}$  is adopted. On the basis of the latest experimental measurements<sup>62</sup>, the latter value is considered more reliable. The surface tension coefficient of stainless steel<sup>63</sup> is approximately  $-4.58 \times 10^{-4} \text{ N m}^{-1} \text{ K}^{-1}$ , which is significantly greater than that of aluminium alloy. The Marangoni force is the product of the surface tension gradient and the temperature gradient. Therefore, at the same temperature gradient, the Marangoni force on the surface of a molten aluminium alloy pool is much smaller than that on the surface of a steel pool. Furthermore, the thermal conductivity of aluminium alloys is significantly greater than that of steel, allowing heat to dissipate more easily and leading to a more gradual temperature gradient. This further indicates that, unlike steel, the Marangoni

force in aluminium alloy melting is relatively weak and does not play a major role in driving metal flow.

Trinh et al.<sup>64</sup> used the two-colour pyrometry method to measure the temperature at different polarities during AC TIG welding and reported that the molten pool centre temperature in the EN phase was significantly higher than that in the EP phase, whereas the temperature at the pool edge remained the same. The temperature distribution curve clearly shows that the temperature gradient in the EN phase is greater than that in the EP phase. Consequently, the Marangoni force under EN polarity is greater than that in the EP phase. If the Marangoni force is the dominant driving force of metal flow, then the molten pool flow velocity in the EN phase should be higher than that in the EP phase. However, this contradicts the experimental results obtained in this study. Therefore, the Marangoni force is not the primary factor driving the flow of metals in the AC arc melting process.

Consequently, it is necessary to focus on the differences in the arc characteristics between positive and negative polarities. The cathode spot phenomenon, occurring only during the EP stage, is a unique phenomenon of AC arcs, and it does not change with the arc state<sup>40</sup>. The cathode spot moves on the workpiece surface and has a very high current density (approximately  $10^{12} \text{ A m}^{-2}$ ), resulting in the generation of tremendous heat and evaporation forces in a short time<sup>42,65,66</sup>. To analyse the effects of the cathode spots on the molten pool, a schematic diagram was created, as shown in Fig. 5c. This is based on the TIG arc melting process and corresponds to the subsequent observation of the molten pool surface. As shown in Fig. 5c, the spot separates from the arc body on the cathode surface and can move at high speed. Owing to the high-temperature characteristics of the spot, a large amount of metal vapour is generated around it. During this process, there are two forces at work: the evaporation reaction force, and the drag force produced by the metal vapour jet. According to estimates by Tanberg<sup>67</sup>, the recoil force of a cathode spot is approximately  $10^4 \text{ N m}^{-2}$ . Additionally, the metal jet velocity generated by the evaporation of a single spot can reach  $100 \text{ m s}^{-1}$ . According to the shear force calculation equation, the shear force exerted on the melt pool by the metal jet from a single spot can reach  $10^3 \text{ N m}^{-2}$ . Although this study focuses on vacuum arc discharges, the cathode spots in welding arcs exhibit similar current densities. As a result, the thermal effects produced are approximately of the same order of magnitude, making them a useful reference. Since the cathode spot expands outwards from the centre of the arc, the pressure is greater at the locations where the spots are present, whereas the areas without spots experience lower pressure. This results in an uneven pressure distribution perpendicular to the molten pool surface. This uneven pressure distribution results in tangential shear forces, as shown in Fig. 5d. The combined action of these two forces creates a shear force on the surface of the melt pool, which ranges from the spot-free zone to the spot-rich zone, thereby driving metal flow. Although the thermal effects of the spots are significant, their size is extremely small, and the dispersed nature of the spots limits the corresponding effects on metal flow.

The plasma cloud created by metal vapour above the spot was monitored, it was found that scattered spots minimally drive the flow of the melt pool because the size of a single spot is small and its range of influence is limited. However, when the spots are clustered to a certain extent and move, the metal in the melt pool flows rapidly, as shown in Fig. 5e and Supplementary Movie 5. Although it is challenging to obtain clear images of both the plasma cloud and the molten pool under the same observation conditions, the images that can illustrate the dynamic process of both were obtained by carefully adjusting the laser intensity and focal level and by using optical filters. Before 3.0 ms, the cathode spots are dispersed, and there is no flow in the molten pool. The cathode spots subsequently aggregate into clusters, which can be observed through the generated metal vapour. The clusters of spots then move in a specific direction, and at this point, the molten metal significantly moves. To clearly illustrate the movement of the plasma cloud generated by the spot clusters, the images at 3.6 and 6.0 ms are been magnified, as shown in Fig. 5f, g. The white region above the molten pool, resembling a cloud, represents the plasma cloud generated by the spot clusters. The magnified image at 3.6 ms, shows that the plasma cloud is



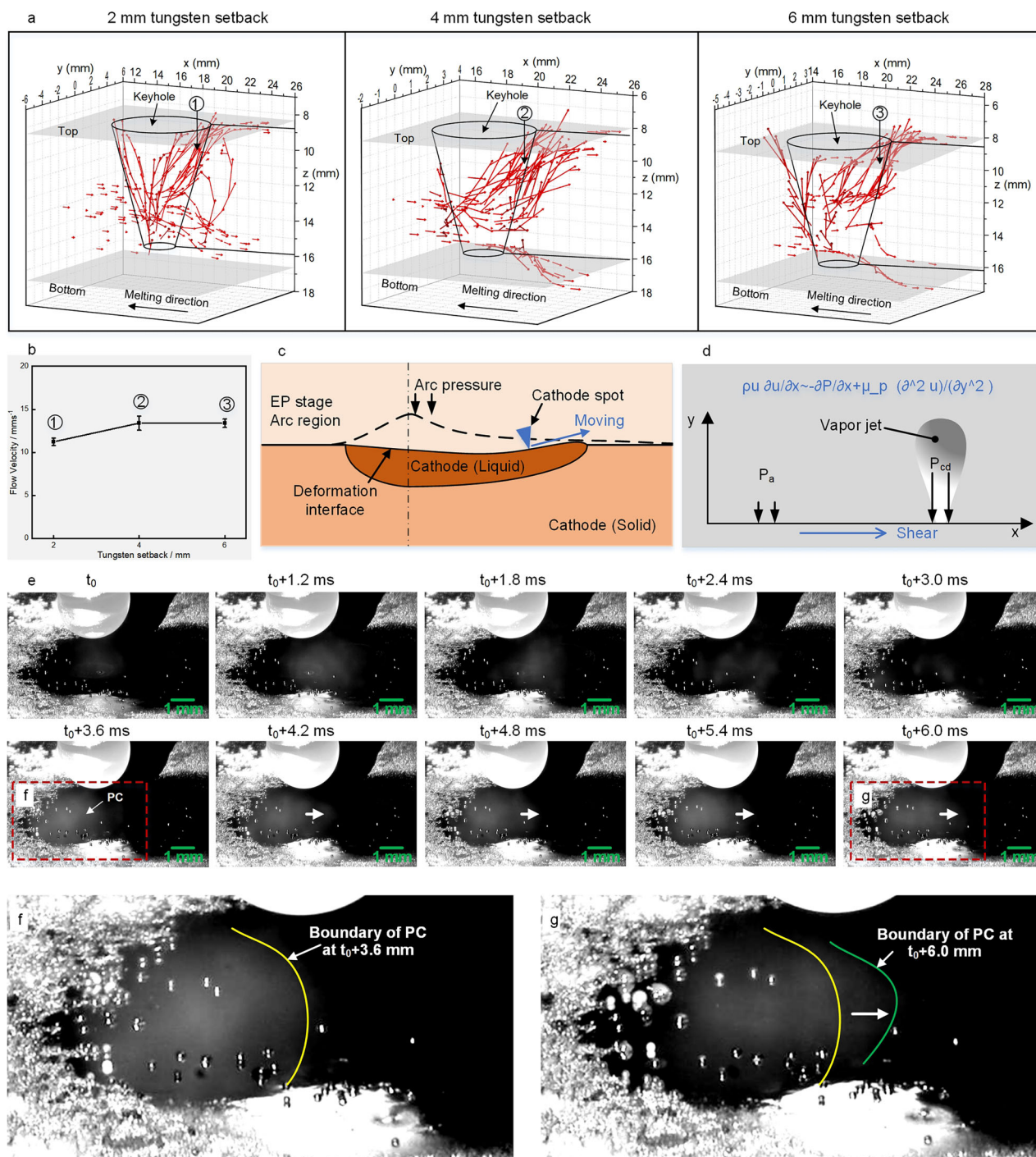


**Fig. 5 | Analysis of the cathode spot driven mechanism for polarity-dependent flow differences during AC arc melting of aluminium alloy.** **a** Three-dimensional convection of the keyhole molten pool with different tungsten setbacks. The arrowed lines represent the flow vectors on each trajectory. Multiple flow trajectories together form the overall flow field of the molten pool. **b** Average flow velocity at the keyhole back sidewall. The numbers (①, ②, ③) correspond to those in **a**. **c** Schematic of

cathode spot movement on the molten pool surface. **d** Schematic illustrating the shear caused by vapour jet because of cathode spot. **e** Movement of the plasma cloud caused by clusters of cathode spots.  $t_0$  represents the start moment of EP stage. Panels **f**, **g** are magnified images showing the boundaries of the plasma cloud. Error bars represent one standard deviation (SD) from the mean. PC denotes 'plasma cloud'.

concentrated on the left side of the image and then gradually moves to the right, accompanied by the movement of tracer particles in the same direction. This clearly demonstrates the phenomenon of spot clusters driving metal flow.

In summary, our research revealed a unique but often overlooked phenomenon during the AC arc melting of aluminium alloys. The flow velocity of liquid metal in the molten pool during the EP phase is significantly higher than that in the EN phase. This phenomenon cannot be

explained by conventional arc melting theories, making it challenging to understand. Through advanced observational methods, we determined that during the EP phase, cathode spots cluster and move in a specific direction, generating a pressure gradient on the surface of the liquid metal. The uneven surface pressure distribution of the molten pool caused by spot clusters and the shear force of the plasma cloud are the main factors influencing molten pool flow during AC arc melting. This in-depth investigation provides a solid foundation for improving the quality and efficiency of aluminium alloy

welding and additive manufacturing processes. Additionally, this study contributes valuable insights to the field of high-temperature fluid dynamics. Furthermore, this research provides a basis for future research in some directions, such as studying the motion characteristics of cathode spots and leveraging their controllability to manage molten pool flow and manufacturing defects in aluminium alloy processing. This work also paves the way for achieving more precise control of AC arc melting processes in the future.

## Methods

### Materials and melting process

A5052P (type number in the Japanese Industrial Standards) aluminium alloy rectangular substrates (150 mm long  $\times$  100 mm wide  $\times$  5, 8 and 10 mm thick) were used for molten pool surface flow measurements and X-ray imaging experiments. The thicknesses of the base metal were 5, 8, and 10 mm. The A5052P aluminium alloy had a nominal chemical composition (wt. %) of Si-0.25, Fe-0.40, Cu-0.10, Mn-0.10, Mg-(2.2 ~ 2.8), Cr-(0.15–0.35), Zn-0.10, and Al balance. The substrates for molten pool surface flow observation were polished, and the surface with treated coarse silicon carbide sandpaper to prevent laser reflection. A plasma arc melting machine with a square waveform, NW-300ASR (Nippon Steel Welding & Engineering Co., Ltd., Tokyo, Japan), was adopted as the power supply to obtain two kinds of molten pools: a keyhole molten pool and a blind keyhole molten pool. The substrates were melted by the high temperature of the plasma arc, and a keyhole formed if the arc forces were large. A blind keyhole formed if the forces were small. A schematic of the plasma arc torch structure is shown in Fig. 1. A small torch with a maximum current of 200 A (N-101WH, Nippon Steel) was used for the 5 mm-thick aluminium alloy, and a large torch (N-504WH) with a maximum current of 300 A was used for the 8 and 10 mm-thick aluminium alloys. The torch and the power supply were connected by cables, and a plasma arc formed between the torch and the substrate.

The following parameters were adopted for the keyhole plasma arc melting process: tungsten diameter, 3.2 mm; nozzle diameter, 2.8 mm; plasma gas flow rate, 1.45 L min<sup>-1</sup>; shielding gas flow rate, 10 L min<sup>-1</sup>; current in the EP phase, 150 A; current in the EN phase, 150 A; AC current frequency, 40 Hz; duty ratio in the EN phase, 70%; standoff, 2 mm; tungsten setback, 3 mm; and welding speed, 4.5 mm s<sup>-1</sup>. For melting 8 mm-thick aluminium alloy, the tungsten diameter was 4.8 mm, the tungsten setback was 4 mm, the nozzle diameter was 4.0 mm, the plasma gas flow rate was 2.5 L min<sup>-1</sup>, the shielding gas flow rate was 10 L min<sup>-1</sup>, the current of the EP was 205–210 A, the current in the EN phase was 200–205 A, the AC current frequency was 40 Hz, the duty ratio in the EN phase was 70%, the standoff was 2 mm, and the welding speed was 3.2 mm s<sup>-1</sup>. Compared with the parameters for melting 8 mm-thick aluminium alloy, the current in the EP stage was 230–240 A and the current in the EN stage was 230–240 A for 10 mm-thick aluminium alloy, and the other parameters were the same. For soft plasma arc melting, the parameters used were as follows: current duration ratio (EN 75%, EP 25%), current (EN 120 A, EP 120 A), diameter of the tungsten electrode (4.8 mm), plasma gas flow rate (2.0 L min<sup>-1</sup>), shielding gas flow rate (10.0 L min<sup>-1</sup>), melting speed (1 mm s<sup>-1</sup>), and tungsten setback (2.0 mm).

A tungsten inert gas (TIG) melting machine with a square waveform, namely, a Miller Dynasty 700 (Miller Electric Mfg. Co., Appleton, WI 54914 USA), was adopted to form a molten pool with small deformation. The parameters for this experiment were as follows: current duration ratio (EN 75%, EP 25%), current (EN 150 A, EP 150 A), diameter of the tungsten electrode (3.2 mm), shielding gas flow rate (10.0 L min<sup>-1</sup>), and melting speed (2 mm s<sup>-1</sup>).

### Dual X-ray 4-dimensional imaging

The internal flow experiments for the molten pool were performed at the Joining and Welding Research Institute of Osaka University. A schematic of the X-ray experiment is shown in Fig. 2a. The system includes two pairs of X-rays and a high-speed camera. The spatial positions of the cameras and

the X-ray devices were adjusted with four robotic arms (NACHI Co., Ltd., JP) before the experiments. X-rays were generated by two X-ray tubes<sup>68</sup> passing through the observation area of the metal, yielding an image at the front end of the camera lens. The X-ray imaging system used in this study was jointly developed and manufactured by Toshiba Corporation of Japan and the Joining and Welding Research Institute of Osaka University. We do not describe its principles in detail and simply use this system to obtain information about the internal flow within the molten pool. The angle of the X-ray with respect to the horizontal direction was 30°. Two X-rays intersected at the point where the substrates were placed. During the experiments, the two cameras and X-rays were fixed, and the substrates moved in the melting direction at a set speed (3.0–3.5 mm s<sup>-1</sup>), driven by the moving trolley. The maximum tube voltage of the mini-focused X-ray source was 230 kV, and the maximum tube current was 1000  $\mu$ A, whereas the maximum tube voltage of the micro-focused X-ray source was 225 kV, and the maximum tube current was 3.5 mA. During the experiment, the following X-ray energy was used: (170 kV, 500  $\mu$ A) for the mini-focused source and (100 kV, 2.6 mA) for the micro-focused source for the 5 mm case; (180 kV, 700  $\mu$ A) for the mini-focused source and (100 kV, 3.0 mA) for the micro-focused source for the 8 mm case; and (190 kV, 700  $\mu$ A) for the mini-focused source and (140 kV, 3.0 mA) for the micro-focused source for the 10 mm case. The target element of the two X-ray sources was tungsten. The image resolution was 800  $\times$  600 pixels, corresponding to a physical size of 22 mm  $\times$  20 mm. The temporal resolution was 0.5 ms. The frame rate was 2000 fps. The exposure time of both imaging systems was 498  $\mu$ s. For safety, the equipment was placed in a room enclosed by a lead sheet, and the operator watched the interior and controlled the equipment from outside the room with the help of a surveillance camera.

### Pulse laser and high-speed camera imaging

Simultaneous imaging with the laser and high-speed camera was used to monitor the flow at the surface of the molten pool. Zirconia with a diameter of 0.03 mm was used as the tracer. The density was 5.85 g cm<sup>-3</sup>, and the melting point was 2973 K. A small hole with a diameter of 1 mm and depth of 2 mm was pre-drilled at the top and bottom of the workpiece before each experiment. The zirconia particles were placed inside the small hole, and then the hole was sealed with aluminium alloy wire. In addition, slag with a diameter of approximately 0.05 mm on the molten pool surface was selected to observe the region without zirconia. Common components of the slag of the A5052P aluminium alloy include the oxides of aluminium and magnesium with high melting points (above 2300 K) and low densities (below 4 g cm<sup>-3</sup>) floating on the surface of the weld pool. The movement of slag was indicative of the flow of the weld pool surface. The origin point was then defined to obtain the two-dimensional coordinates of each particle. The moving distance of a particle was divided by a time interval over two consecutive images to obtain its velocity. A high-speed camera was used to capture 2000 pictures of the weld pool per second. The positions of the particles on the weld pool surface, including the slag and zirconia, were different in these images. The trajectory was obtained by connecting the different positions of one particle in each image. Different trajectories were obtained by tracking different particles. On the basis of the weld pool images, the origin coordinate was set at the centre of the weld bead. Thus, the trajectories with different relative positions on the weld pool surface were correspondingly located. The trajectory and velocity of the particles were considered the same as those of the liquid metal because the motion of the particles was due to liquid metal flow. By analysing the flow process of as many particles as possible, the liquid metal flow at different positions around the keyhole was obtained.

### Numerical simulation model

The arc plasma flow velocity was simulated via a magnetohydrodynamic model. The calculation domain included the tungsten electrode, constraint nozzle, shielding gas nozzle, plasma arc region and base metal. The keyhole was pre-set on the basis of the experimental results when the geometric model was established. The calculation process did not include the



deformation of the free surface of the molten pool. The parameters were the same as those used in the experimental welding of a 10 mm-thick aluminium alloy. Since the primary purpose of the calculation was to explore the high flow velocity of the plasma and roughly estimate the shear force, other aspects of the welding process were not simulated. The three governing equations, namely, continuity, momentum, and energy conservation, were applied with the finite volume method. The momentum source term was the Lorentz force, and the energy source term was Joule heating. The calculation required the current density, magnetic field strength, and electric field strength, which were obtained by solving Maxwell's equations. In ANSYS Fluent, UDS was first defined to store the vector potential and electric potential, and the equation set was solved on the basis of the Poisson equation. The electric field strength and current density were derived from the electric potential. The magnetic induction intensity was obtained from the vector potential. The Lorentz force was determined using the current density and magnetic field strength. Joule heating was calculated on the basis of the current density and electric field strength. Ultimately, the distributions of the arc's flow field, temperature field, and electromagnetic field were obtained. The fluid flow was assumed to be incompressible, turbulent, and Newtonian. The thermophysical properties of the base metal and gas were temperature dependent and calculated via JMatpro software. Further details about these models can be found in the literature<sup>69,70</sup>.

### Data availability

The data supporting the findings of this work is available in the main text and supplementary movies. Raw data are available from the corresponding author Fan Jiang on reasonable request.

Received: 5 February 2024; Accepted: 29 April 2025;

Published online: 08 May 2025

### References

- Pollock, T. M. Alloy design for aircraft engines. *Nat. Mater.* **15**, 809–815 (2016).
- Martin, J. H. et al. 3D printing of high-strength aluminium alloys. *Nature* **549**, 365–369 (2017).
- Sokoluk, M., Cao, C., Pan, S. & Li, X. Nanoparticle-enabled phase control for arc welding of unweldable aluminum alloy 7075. *Nat. Commun.* **10**, 98 (2019).
- Tashiro, S., Miyata, M. & Tanaka, M. Numerical analysis of AC tungsten inert gas welding of aluminum plate in consideration of oxide layer cleaning. *Thin Solid Films* **519**, 7025–7029 (2011).
- He, H. et al. Flux modification for AC-TIG braze welding of aluminium to stainless steel. *Sci. Technol. Weld. Join.* **19**, 527–533 (2014).
- Zhang, Z., Liu, L., Sun, H. & Wang, L. AC TIG welding with single-component oxide activating flux for AZ31B magnesium alloys. *J. Mater. Sci.* **43**, 1382–1388 (2008).
- Li, Y., Tian, S., Wu, C. S. & Tanaka, M. Experimental sensing of molten flow velocity, weld pool and keyhole geometries in ultrasonic-assisted plasma arc welding. *J. Manuf. Process* **64**, 1412–1419 (2021).
- Wang, L., Chen, J., Wu, C. & Gao, J. Backward flowing molten metal in weld pool and its influence on humping bead in high-speed GMAW. *J. Mater. Process Technol.* **237**, 342–350 (2016).
- Wang, L., Wu, C., Chen, J. & Gao, J. Experimental measurement of fluid flow in high-speed GMAW assisted by transverse magnetic field. *J. Manuf. Process* **56**, 1193–1200 (2020).
- Nakamura, H., Kawahito, Y., Nishimoto, K. & Katayama, S. Elucidation of melt flows and spatter formation mechanisms during high power laser welding of pure titanium. *J. Laser Appl.* **27**, 032012 (2015).
- Van Anh, N., Tashiro, S., Van Hanh, B. & Tanaka, M. Experimental investigation on the weld pool formation process in plasma keyhole arc welding. *J. Phys. D: Appl Phys.* **51**, 015204 (2018).
- Morisada, Y., Fujii, H., Kawahito, Y., Nakata, K. & Tanaka, M. Three-dimensional visualization of material flow during friction stir welding by two pairs of X-ray transmission systems. *Scr. Mater.* **65**, 1085–1088 (2011).
- Miyagi, M., Kawahito, Y., Kawakami, H. & Shoubu, T. Dynamics of solid-liquid interface and porosity formation determined through x-ray phase-contrast in laser welding of pure Al. *J. Mater. Process Technol.* **250**, 9–15 (2017).
- Leung, C. L. A. et al. In situ X-ray imaging of defect and molten pool dynamics in laser additive manufacturing. *Nat. Commun.* **9**, 1355 (2018).
- Hojjatadeh, S. M. H. et al. Pore elimination mechanisms during 3D printing of metals. *Nat. Commun.* **10**, 3088 (2019).
- Huang, Y. et al. Keyhole fluctuation and pore formation mechanisms during laser powder bed fusion additive manufacturing. *Nat. Commun.* **13**, 1170 (2022).
- Cunningham, R. et al. Keyhole threshold and morphology in laser melting revealed by ultrahigh-speed x-ray imaging. *Science* (1979) **363**, 849–852 (2019).
- Zhao, C. et al. Critical instability at moving keyhole tip generates porosity in laser melting. *Science* (1979) **370**, 1080–1086 (2020).
- Ren, Z. et al. Machine learning-aided real-time detection of keyhole pore generation in laser powder bed fusion. *Science* (1979) **379**, 89–94 (2023).
- Miyagi, M. & Wang, J. Keyhole dynamics and morphology visualized by in-situ X-ray imaging in laser melting of austenitic stainless steel. *J. Mater. Process Technol.* **282**, 116673 (2020).
- Li, W. et al. AM-SegNet for additive manufacturing in situ X-ray image segmentation and feature quantification. *Virtual Phys. Prototyp.* **19**, e2325572 (2024).
- Lowke, J. J. & Tanaka, M. LTE-diffusion approximation' for arc calculations. *J. Phys. D: Appl Phys.* **39**, 3634–3643 (2006).
- Ogino, Y., Hirata, Y. & Murphy, A. B. Numerical simulation of GMAW process using Ar and an Ar–CO<sub>2</sub> gas mixture. *Weld. World* **60**, 345–353 (2016).
- Tanaka, M. & Lowke, J. J. Predictions of weld pool profiles using plasma physics. *J. Phys. D: Appl Phys.* **40**, R1–R23 (2007).
- Murphy, A. B. et al. Modelling of arc welding: The importance of including the arc plasma in the computational domain. *Vacuum* **85**, 579–584 (2010).
- Tanaka, M., Ushio, M. & Lowke, J. J. Numerical study of gas tungsten arc plasma with anode melting. *Vacuum* **73**, 381–389 (2004).
- Limmaneevichitr, C. & Kou, S. Visualization of Marangoni Convection in Simulated Weld Pools. *Weld. J.* **79**, 126–135 (2000).
- Aucott, L. et al. Revealing internal flow behaviour in arc welding and additive manufacturing of metals. *Nat. Commun.* **9**, 5414 (2018).
- Kah, P., Suoranta, R. & Martikainen, J. Advanced gas metal arc welding processes. *Int. J. Adv. Manuf. Technol.* **67**, 655–674 (2013).
- Arif, N. & Chung, H. Alternating current-gas metal arc welding for application to thin sheets. *J. Mater. Process Technol.* **214**, 1828–1837 (2014).
- Arif, N. & Chung, H. Alternating current-gas metal arc welding for application to thick plates. *J. Mater. Process Technol.* **222**, 75–83 (2015).
- Wang, Y., Qi, B., Cong, B., Yang, M. & Liu, F. Arc characteristics in double-pulsed VP-GTAW for aluminum alloy. *J. Mater. Process Technol.* **249**, 89–95 (2017).
- Rose, S. et al. Arc attachments on aluminium during tungsten electrode positive polarity in TIG welding of aluminium. in 91–99 (IIW SG-212, 2011).
- Cho, J., Lee, J. J. & Bae, S. H. Heat input analysis of variable polarity arc welding of aluminum. *Int J. Adv. Manuf Technol.* **81**, 1273–1280 (2015).

35. Xu, B., Tashiro, S., Jiang, F., Tanaka, M. & Chen, S. The effect of electrode energy balance on variable polarity plasma arc pressure. *Int J. Heat. Mass Transf.* **145**, 118715 (2019).
36. Li, J., Wang, L., Gao, H., Zhang, X. & Zhang, R. Numerical simulation of the interaction between double cathode spot craters in vacuum arc. *Phys. Plasmas* **28**, 123506 (2021).
37. Liu, L., Liu, S., Yuan, Z. & Chen, L. The motion and distribution characteristics of cathode spot and its influence on plasma parameters. *Vacuum* **215**, 112394 (2023).
38. Juttner, B. Characterization of the cathode spot. *IEEE Trans. Plasma Sci.* PS-15, 474–480 (1987).
39. Bystrov, Y. A., Kostin, D. K., Lisenkov, A. A. & Vetrov, N. Z. Cathode spots of vacuum arc discharges: Motion control on the working surface. *Vak. Forsch. und Prax.* **27**, 22–25 (2015).
40. Burkhard, J. Cathode spots of electric arcs. *J. Phys. D: Appl. Phys.* **34**, 103–123 (2001).
41. Puchkarev, V. F. & Bochkarev, M. B. Cathode spot initiation under plasma. *J. Phys. D: Appl. Phys.* **27**, 1214–1219 (1994).
42. Phan, L. H. et al. Influence of shielding gas on cathode spot behaviours in alternating current tungsten inert gas welding of aluminium. *Sci. Technol. Weld. Join.* **25**, 258–264 (2020).
43. Phan, L. H. et al. Investigating cathode spot behavior in argon alternating current tungsten inert gas welding of aluminum through experimental observation. *J. Phys. D: Appl. Phys.* **52**, 26LT02 (2019).
44. Jeong, H., Park, K., Baek, S. & Cho, J. Thermal efficiency decision of variable polarity aluminum arc welding through molten pool analysis. *Int J. Heat. Mass Transf.* **138**, 729–737 (2019).
45. Pan, J., Hu, S., Yang, L. & Wang, D. Investigation of molten pool behavior and weld bead formation in VP-GTAW by numerical modelling. *Mater. Des.* **111**, 600–607 (2016).
46. Jiang, F., Li, C. & Chen, S. Experimental investigation on heat transfer of different phase in variable polarity plasma arc welding. *Weld. World* **63**, 1153–1162 (2019).
47. Xu, B., Tashiro, S., Tanaka, M., Jiang, F. & Chen, S. Physical mechanisms of fluid flow and joint inhomogeneity in variable-polarity plasma arc welding of thick aluminum alloy plates. *Phys. Fluids* **33**, 087103 (2021).
48. Zhou, W., Jia, C., Zhou, F. & Wu, C. Dynamic evolution of keyhole and weld pool throughout the thickness during keyhole plasma arc welding. *J. Mater. Process Technol.* **322**, 118206 (2023).
49. Liu, Z. M. et al. Plasma arc welding: Process variants and its recent developments of sensing, controlling and modeling. *J. Manuf. Process* **23**, 315–327 (2016).
50. Tashiro, S. Interaction mechanism of arc, keyhole, and weld pool in keyhole plasma arc welding: A review. *Materials* **17**, 1348 (2024).
51. Pan, J., Hu, S., Yang, L. & Chen, S. Numerical analysis of the heat transfer and material flow during keyhole plasma arc welding using a fully coupled tungsten–plasma–anode model. *Acta Mater.* **118**, 221–229 (2016).
52. Xu, B. et al. Material flow analyses of high-efficiency joint process in VPPA keyhole flat welding by X-ray transmission system. *J. Clean. Prod.* **250**, 119450 (2020).
53. Meng, X., Qin, G. & Zou, Z. Sensitivity of driving forces on molten pool behavior and defect formation in high-speed gas tungsten arc welding. *Int J. Heat. Mass Transf.* **107**, 1119–1128 (2017).
54. Meng, X., Qin, G. & Zou, Z. Investigation of humping defect in high speed gas tungsten arc welding by numerical modelling. *Mater. Des.* **94**, 69–78 (2016).
55. Wu, D., Van Nguyen, A., Tashiro, S., Hua, X. & Tanaka, M. Elucidation of the weld pool convection and keyhole formation mechanism in the keyhole plasma arc welding. *Int J. Heat. Mass Transf.* **131**, 920–931 (2019).
56. Xu, B., Tashiro, S., Jiang, F., Chen, S. & Tanaka, M. Effect of arc pressure on the digging process in variable polarity plasma arc welding of A5052P aluminum alloy. *Materials* **12**, 1071 (2019).
57. Fang, L. et al. Measurement of interfacial shear stress in gas-liquid two-phase stratified flow. *J. Appl. Phys.* **134**, 164703 (2023).
58. Masson, A. & Nykyri, K. Kelvin–Helmholtz instability: lessons learned and ways forward. *Space Sci. Rev.* **214**, 71 (2018).
59. Li, L., Peng, G., Wang, J., Gong, J. & Meng, S. Numerical and experimental study on keyhole and melt flow dynamics during laser welding of aluminium alloys under subatmospheric pressures. *Int J. Heat. Mass Transf.* **133**, 812–826 (2019).
60. Chen, G., Liu, J., Shu, X., Gu, H. & Zhang, B. Numerical simulation of keyhole morphology and molten pool flow behavior in aluminum alloy electron-beam welding. *Int J. Heat. Mass Transf.* **138**, 879–888 (2019).
61. Wang, H. X., Wei, Y. H. & Yang, C. L. Numerical simulation of variable polarity vertical-up plasma arc welding process. *Comput. Mater. Sci.* **38**, 571–587 (2007).
62. Fukuyama, H., Higashi, H., Adachi, M. & Ohtsuka, M. Density and surface tension measurements of molten Al-Si based alloys. *High. Temp. Mater. Process.* **42**, 20220286 (2023).
63. Tanaka, M., Terasaki, H., Ushio, M. & Lowke, J. J. Numerical study of a free-burning argon arc with anode melting. *Plasma Chem. Plasma Process.* **23**, 585–606 (2003).
64. Trinh, Q. N., Phan, L. H., Tashiro, S., Bui, V. H. & Tanaka, M. Optical measurement of surface temperature distribution of weld pool in AC tungsten inert gas welding of aluminum A1050. *J. Smart Process.* **8**, 213–218 (2019).
65. Wang, L., Zhang, X., Li, J., Luo, M. & Jia, S. Study of cathode-spot crater and droplet formation in a vacuum arc. *J. Phys. D: Appl. Phys.* **54**, 215202 (2021).
66. Mesyats, G. A. & Uimanov, I. V. Semiempirical model of the microcrater formation in the cathode spot of a vacuum arc. *IEEE Trans. Plasma Sci.* **45**, 2087–2092 (2017).
67. Tanberg, R. On the cathode of an arc drawn in vacuum. *Phys. Rev.* **35**, 1080–1089 (1930).
68. Tabakov, S. *College on Medical Physics. Digital Imaging Science and Technology to Enhance Healthcare in the Developing Countries.* (2010).
69. Jian, X., Wu, C. S., Zhang, G. & Chen, J. A unified 3D model for an interaction mechanism of the plasma arc, weld pool and keyhole in plasma arc welding. *J. Phys. D: Appl. Phys.* **48**, 465504 (2015).
70. Wu, D., Tashiro, S., Hua, X. & Tanaka, M. Coupled mechanisms of the keyhole, energy transfer and compositional change associated with the variable polarity plasma arc process. *J. Phys. D: Appl. Phys.* **54**, 115204 (2021).

## Acknowledgements

This work was supported by the National Natural Science Foundation of China (Grant No. 52375301), National Natural Science Foundation of China (Grant Nos. 52275302 and 52322508), National Key Research and Development Programme of China (2023YFB3407701).

## Author contributions

B.X. and C.Z. performed the experiments and data processing. G.Z. and F.J. designed and supervised the experiments (laser and HSVI). S.T. and M.T. designed and supervised the experiments (X-ray radiography). B.X. analyzed the data and drafted the original manuscript. F.J., S.T. and S.C. supervised the data analysis and secured the funding support. B.X., F.J., S.C. and S.T. assisted in discussion of mechanisms. B.X. and F.J. reviewed and revised the manuscript. F.J. and S.C. supervised the entire project.

## Competing interests

The authors declare no competing interests.

## Additional information

**Supplementary information** The online version contains supplementary material available at <https://doi.org/10.1038/s43246-025-00819-x>.

**Correspondence** and requests for materials should be addressed to Fan Jiang or Shujun Chen.

**Peer review information** *Communications Materials* thanks the anonymous reviewers for their contribution to the peer review of this work. Primary Handling Editor: John Plummer. A peer review file is available.

**Reprints and permissions information** is available at <http://www.nature.com/reprints>

**Publisher's note** Springer Nature remains neutral with regard to jurisdictional claims in published maps and institutional affiliations.

**Open Access** This article is licensed under a Creative Commons Attribution-NonCommercial-NoDerivatives 4.0 International License, which permits any non-commercial use, sharing, distribution and reproduction in any medium or format, as long as you give appropriate credit to the original author(s) and the source, provide a link to the Creative Commons licence, and indicate if you modified the licensed material. You do not have permission under this licence to share adapted material derived from this article or parts of it. The images or other third party material in this article are included in the article's Creative Commons licence, unless indicated otherwise in a credit line to the material. If material is not included in the article's Creative Commons licence and your intended use is not permitted by statutory regulation or exceeds the permitted use, you will need to obtain permission directly from the copyright holder. To view a copy of this licence, visit <http://creativecommons.org/licenses/by-nc-nd/4.0/>.

© The Author(s) 2025